A hexagon based Mn(ii) rod metal-organic framework - structure, SF<inf>6</inf> gas sorption, magnetism and electrochemistry

Citation for the original published paper (version of record):
Amombo Noa, F., Cheung, O., Åhlén, M. et al (2023). A hexagon based Mn(ii) rod metal-organic framework - structure, SF<inf>6</inf> gas sorption,
magnetism and electrochemistry. Chemical Communications, 59(15): 2106-2109.
http://dx.doi.org/10.1039/d2cc06916d

(article starts on next page)

ChemComm

COMMUNICATION

View Article Online
View Journal

Check for updates

Cite this: DOI: 10.1039/d2cc06916d

Received 19th December 2022,
Accepted 25th January 2023

DOI: 10.1039/d2cc06916d

rsc.li/chemcomm

A hexagon based Mn(II) rod metal–organic framework – structure, SF_6 gas sorption, magnetism and electrochemistry†

Francoise M. Amombo Noa,*[a] Ocean Cheung,[b] Michelle Åhlén,[b] Elisabet Ahlberg,[c] Priyanka Nehla,[b] Germán Salazar-Alvarez,[b] Soheil Ershadrad,[d] Biplab Sanyal[d] and Lars Öhrström*[a]

A manganese(II) metal–organic framework based on the hexatopic hexakis(4-carboxyphenyl)benzene, cpb^{6-}: $[Mn_3(cpb)(dmf)_3]$, was solvothermally prepared showing a Langmuir area of 438 $m^2\ g^{-1}$, rapid uptake of sulfur hexafluoride (SF_6) as well as electrochemical and magnetic properties, while single crystal diffraction reveals an unusual rod-MOF topology.

Metal–Organic Frameworks, colloquially known as MOFs,[1] are coming of age with advanced[2] and basic[3] textbooks published, and gas storage devices on the market with other applications close to commercialization.[4] An emerging application is the capture of SF_6, a greenhouse gas some 22 000 times more potent than CO_2, used in industrial settings because of its dielectric properties, its non-toxicity, and thermal stabilty.[5,6]

Manganese(II) is an attractive choice for such MOF construction as it is ubiquitous, non-toxic and present in relatively high amounts in most living systems. It is also a less common MOF metal ion, compared to *i.e.* Zn(II).[7] In contrast to zinc(II) it is also magnetically and electrochemically active, properties that have recently been investigated.[8] Higher stability may be induced in such MOFs by having the metal secondary building units (SBUs) forming an infinite rod.[9,10]

Here we explore Mn(II) with the hexatopic linker hexakis(4-carboxyphenyl)benzene, cpb^{6-}, Fig. 1. This hexagon shaped linker,[11] has earlier led us to investigate unique topological properties,[12] and recently we implicated the concerted movement of the six carboxyphenyl groups in gate opening CO_2 gas sorption dynamics in a rod-MOF.[13] We noted that the size of the rhombic channels formed by pairwise stacks of cpb linkers would probably conform to the 7 Å diameter suggested as optimal for SF_6 capture,[14] and therefore targeted this greenhouse gas in the present gas sorption study.

Solvothermal synthesis in dimethylformamide (dmf) at 120 °C gave the MOF $[Mn_3(cpb)(dmf)_3]$, **CTH-18**, in good yield. Contrary to some other M(II) cpb MOFs that form 2D kgd-nets with counter ions partly blocking the pores[12] the single crystal structure of **CTH-18** shows an infinite rod metal SBU pairwise connecting the six-connected cpb linkers creating two types of channels running parallel with the rods having approximate minimal dimensions 4.3 × 6.0 Å and 3.4 × 4.7 Å when the van der Waals radii have been excluded. Thus, every Mn(II) only connects to four cpb linkers thereby maintaining a neutral framework, see Fig. 2 and Fig. S1 (ESI†).

CTH-18 is stable in organic solvents including ethanol, unstable in 1 M NaOH(aq) and transforms to other crystalline phases in 1 M HCl and deionized water. Thermogravimetric studies in air indicated gradual solvent loss from the framework below 300 °C, and rapid breakdown of the MOF at 425 °C.

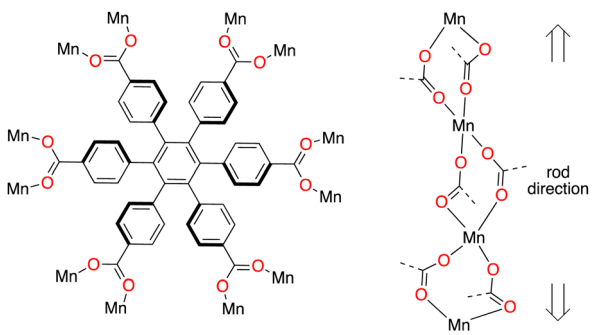

Fig. 1 The linker 1,2,3,4,5,6-hexakis(4-carboxyphenyl) benzene, cpb^{6-}, and how it is connected to a MOF in $[Mn_3(cpb)(dmf)_3]$, **CTH-18**.

[a] Chemistry and Biochemistry, Department of Chemistry and Chemical Engineering, Chalmers University of Technology, Gothenburg SE-41296, Sweden. E-mail: mystere@chalmers.se, ohrstrom@chalmers.se
[b] Department of Materials Science and Engineering, Ångström Laboratory, Uppsala University, Uppsala SE-751 03, Sweden
[c] Department of Chemistry & Molecular Biology, University of Gothenburg, Gothenburg 405 30, Sweden
[d] Department of Physics & Astronomy, Uppsala University, Box-516, Uppsala 75120, Sweden

† Electronic supplementary information (ESI) available: Crystallographic information files, details of synthesis, characterisation, DFT calculations and topology analysis. CCDC 2226584. For ESI and crystallographic data in CIF or other electronic format see DOI: https://doi.org/10.1039/d2cc06916d

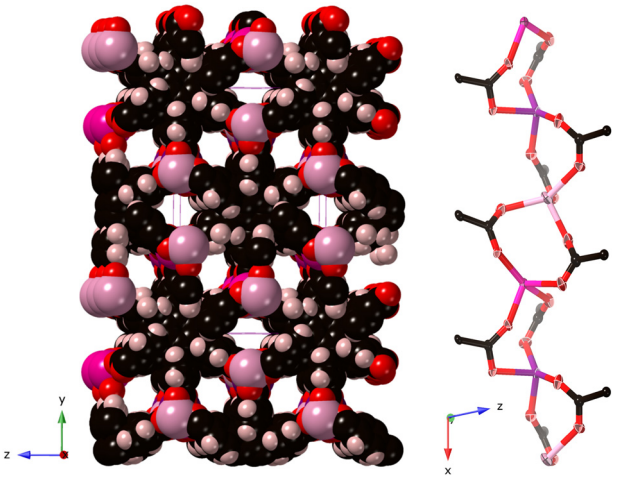

Fig. 2 X-Ray single crystal structure of $[Mn_3(cpb)(dmf)_3]$, **CTH-18** with symmetry independent Mn atoms drawn in different shades of mauve. Gas sorption indicate the severely disordered dmf molecules can be removed by dynamic vacuum, and these have therefore been excluded for clarity. Left: View of the channels using van der Waals radii. Structure and gas sorption indicate apertures of around 5–7 Å. Right: Thermal ellipsoid drawing of the rod metal-SBU showing how the linkers connect pairwise to form the rod.

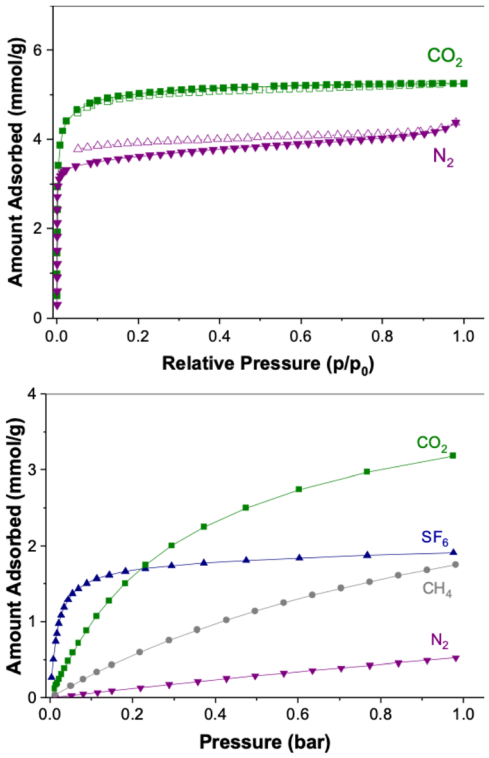

Fig. 3 Top: N_2 (−195 °C) and CO_2 (−78 °C) adsorption and desorption isotherms of $[Mn_3(cpb)(dmf)_3]$, **CTH-18**. Adsorption points are shown as solid symbols and desorption points are shown as hollow symbols. The observed hysteresis on the N_2 desorption isotherm was an artefact of the non-equilibrium adsorption isotherm, caused by very slow N_2 adsorption kinetics on **CTH-18** at −195 °C Bottom: N_2, CH_4, SF_6 and CO_2 adsorption isotherms of **CTH-18** recorded at 20 °C.

Taking the TGA results into account, the material was activated in dynamic vacuum at 250 °C prior to gas sorption analysis. N_2 sorption isotherms recorded at 77 K demonstrated the microporous nature of the material, shown by the steep N_2 adsorption isotherm shape at the very low-pressure regime, Fig. 3 top. However, we noted a very slow N_2 adsorption kinetics on **CTH-18**, especially at low relative pressures. In fact, repeated N_2 sorption experiments yielded different equilibrium uptakes due to this kinetic effect (and the equilibrium N_2 uptake points at low pressures would take several days to reach). The apparent hysteresis shown by the N_2 desorption isotherm was likely to be an artefact of this slow N_2 adsorption rather than N_2 entrapment, *i.e.* N_2 adsorption had not reached equilibrium when recording the adsorption isotherm.

The slow diffusion of N_2 is most likely related to the dimensions of the pore channels being very close to the kinetic diameter of N_2 (3.6 Å). We therefore carried out CO_2 sorption experiments at −78 °C as this molecule has a smaller kinetic diameter (3.3 Å) and thus faster diffusion within these narrow pore channels. Indeed, we did not observe slow CO_2 adsorption kinetics on **CTH-18** and neither hysteresis upon desorption. The specific BET and Langmuir surface area of **CTH-18** estimated using the CO_2 adsorption isotherm were 354 and 438 $m^2\ g^{-1}$, respectively (values estimated using the N_2 isotherm were 289 and 356 $m^2\ g^{-1}$).

The pore size distributions (PSD) were estimated using the CO_2 adsorption isotherm by Density Functional Theory (DFT), with the slit pore model. The DFT PSD of **CTH-18** are plotted in Fig. S2 (ESI†) and showed two distinct types of pores with estimated diameters of ∼4.3 and ∼5.1 Å. The estimated pore diameters should not be taken as accurate numbers but they were in a comparable range to the crystallographic pore sizes of 4.3 × 6.0 Å and 3.4 × 4.7 Å.

The 20 °C N_2, CH_4, SF_6 and CO_2 adsorption isotherms are shown in Fig. 3. **CTH-18** showed selective uptake towards greenhouse gases over N_2. The CO_2 uptake at 1 bar (20 °C) reached over 3.0 mmol g^{-1} with an isosteric heat of CO_2 sorption of around 30–35 kJ mol^{-1} at up to 2.5 mmol g^{-1} loading (Fig. S3, ESI†).

The SF_6 adsorption isotherm showed very sharp increase at low pressures. This sharp increase also indicated that the pore size was close to the kinetic diameter of SF_6 (5.5 Å). As the pore size of **CTH-18** was similar to the size of the kinetic diameter of the adsorbate gas (SF_6), enhanced van der Waals interaction between the pore surface and the adsorbate gas was expected.[6,14,15] The enhanced interaction was reflected by the high isosteric heat of SF_6 adsorption (∼40–50 kJ mol^{-1}).

The greenhouse gas selectivity of **CTH-18** was estimated using $s = (q_1/q_2)/(p_1/p_2)$. The greenhouse gas selectivities were: for CO_2/N_2 ∼ 16 (15% CO_2, 85% N_2), for SF_6/N_2 ∼ 29 (10% SF_6, 90% N_2) and CH_4/N_2 ∼ 3.9 (50% CH_4, 50% N_2). The SF_6/N_2 selectivity of **CTH-18** is thus slightly lower than some highly SF_6 selective MOFs such as Yb-TBAPy or UU-200.[6,14] However, the SF_6 uptake on **CTH-18** at 0.1 bar was higher than many other MOFs, including Zn-MOF-74 (∼1.35 mmol g^{-1} at 298 K)[16]

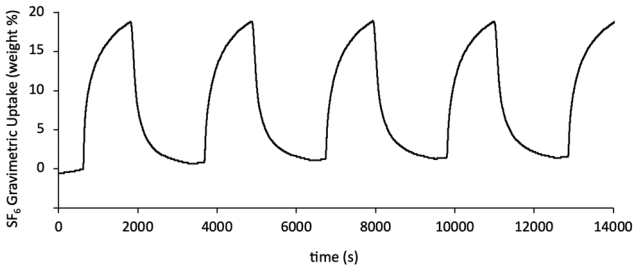

Fig. 4 TGA cyclic SF_6 uptake on **CTH-18**. Adsorption was carried out at 30 °C over 20 minutes, regeneration by heat (desorption) was carried out at 100 °C for 20 minutes.

UiO-66-Zr (~0.75 mmol g^{-1} at 298 K)[17] or SU-100 (~1.08mmol g^{-1} at 298 K).[18]

The SF_6 uptake kinetics on **CTH-18** is shown in Fig. S3 (ESI†) to be reasonably fast, and over 80% of the equilibrium uptake was reached within 600 s. Moreover, **CTH-18** showed high cyclic SF_6 uptake stability (Fig. 4 and Fig. S4, ESI†) with the BET/Langmuir specific area remained unchanged after a number of adsorption/desorption cycles (both with vacuum swing or temperature swing SF_6 adsorption).

Water adsorption/desorption isotherms are shown in Fig. S3 (ESI†) indicating that **CTH-18** has low water uptake at low relative pressures (p/p_0). Two steps in the water uptake were observed at p/p_0 between 0.1 and 0.3. The shape of the water sorption isotherms are comparable to some MOFs that have been investigated for water harvesting,[19] **CTH-18** may thus be interesting for water harvesting applications, although this is beyond the scope of the present study.

Magnetic measurements on Mn(II) MOFs more often than not reveals antiferromagnetic couplings with a few notable exceptions like $[Mn_{12}O_{12}(O_2CR)_{16}(H_2O)_4]$ (R = Me, Et, *etc.*) and other so-called single molecule magnets.[20] There is no reason to anticipate strong coupling through the cpb linker, and in the chain one would predict antiferromagnetic coupling by the relative close proximity of the d^5 Mn(II) ions (*ca.* 4 Å), either directly or through spin polarization of the carboxylate linkers.[21]

This is also what we find for **CTH-18**, the temperature dependence of the magnetisation shows a Néel-like transition at around $T_N \approx 6$ K, Fig. 5. The field-dependent magnetisation curves show the expected linear paramagnetic response in a wide temperature interval, as can be found in Fig. S4 (ESI†).

Calculations based on density functional theory (DFT) reveals an intra-chain antiferromagnetic coupling (5.7 meV Mn^{-1} lower than the ferromagnetic state) between the Mn moments along the x-axis whereas the magnetic coupling between the chains is negligibly small (tens of μeV). The calculated Mn moments were around $4.5\mu_B$, establishing the oxidation state of Mn as 2+.

Electrochemistry has also, but less frequently, been investigated for Mn(II) MOFs.[22–24] We note that an easily accessible Mn(IV) state may be beneficial for water oxidation,[25] but we found no evidence of this in the cyclic voltammetry of **CTH-18** sweeping up to potentials of 1.5 V *vs.* Ag/AgCl (Fig. S7, ESI†).

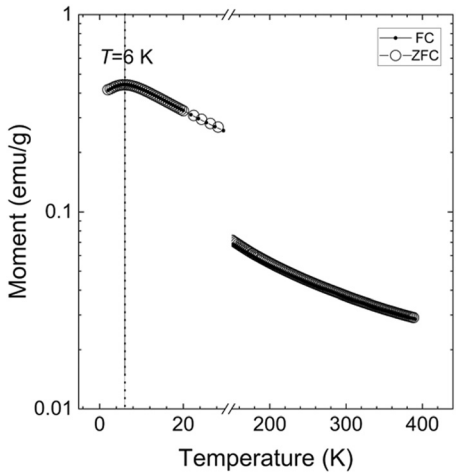

Fig. 5 Temperature dependence of the magnetization for **CTH-18**. An applied field of 1 kOe was used. Below the Néel transition at 6 K we can see the magnetic moment decrease as a result of the antiferromagnetic coupling and above 6 K we see paramagnetic behavior.

The sweep rate dependence in a restricted potential region is shown in Fig. 6.

The redox couple is related to the oxidation of Mn(II) to Mn(III) in the MOF. To simulate the voltammetric response a mechanism separating the electrochemical oxidation and reduction steps was necessary. This is reasonable since the oxidation of Mn(II) to Mn(III) will require that an anion enter the structure.[20] The resulting Mn(III)-anion site is reduced on the negative going scan and the anion leaves. Simulated voltammograms are shown in Fig. S6 (ESI†).

The detailed structure of **CTH-18** shows no unusual features as far as Mn(II) coordination and cpb conformations are concerned,

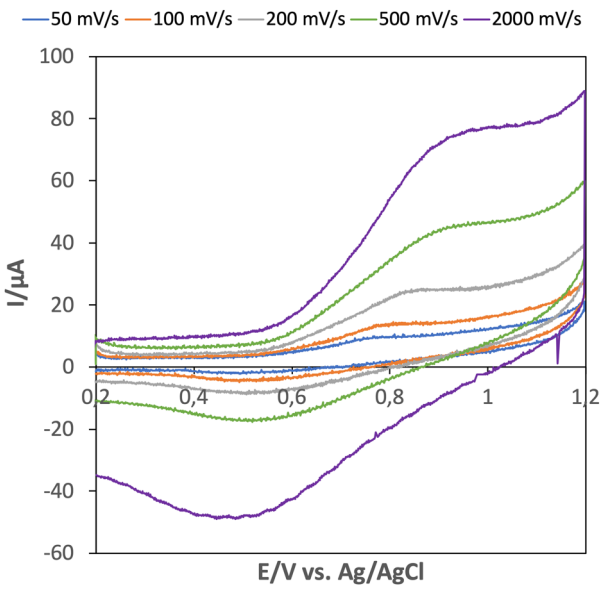

Fig. 6 Cyclic voltammetry at different sweep rates, see legends in phosphate buffer pH = 7. The electrode consisted of carbon paste and $[Mn_3(cpb)(dmf)_3]$, **CTH-18**.

but in contrast to [La_2(cpb)], **CTH-17**[13] the cpb linkers are stacked with a longer spacing (5.7 Å *vs.* 5.5 Å) and linkers with opposite conformational chirality alter in the stacks, see Fig. S8 (ESI†).

The network topology on the other hand, merits a few words. **CTH-18** is an example of a rod-MOF,[26–28] because the metal secondary building unit cannot be reduced to a 0D point forming a dot-MOF, instead it extends in one dimension. However, rod-MOFs pose a descriptive problem as they are commonly analyzed in a different way from dot-MOFs.[26,29,30]

The straight rod, STR, approach is the simplest but even that in this case gives an unusual topology. Each cpb connects pairwise to the same points on the rod giving a three nodal 4- and 6-connected net with point symbol $\{5^2.6^3.7\}\{4.5^2.6^2.7\}\{4.5^4.6^6.7^4\}$ (Fig. S9, ESI†). The more elaborate points-of-extension method that also considers the metal SBU gives a four-nodal six-connected net. Details of the topology assignment can be found in the ESI.†

In conclusion, **CTH-18** shows high SF_6 uptake at 0.1 bar, a pressure practically relevant for SF_6 sorbents, combined with relatively fast kinetics. The SF_6 selectivity compared to N_2 is also higher than for CO_2 and CH_4, and the thermal stability, judged from TGA, is up to 425 °C. It therefore shows some promise for practical applications, shown to be needed by recent reports of industrial safety issues.[31] ‡

We thank the Swedish Research Council (F. M. A. N, L. Ö.), the Olle Engqvist Foundation (F. M. A. N., L. Ö.), Chalmers areas of Advance Energy, Materials, Health and Nano (F. M. A. N.), the Swedish Research Council for Sustainable Development, #2018-00651 and the Swedish Research Council, #2020-04029 (O. C., M. Å.) and #2016-06959 (P. N., G. S. A.), the Chalmers Materials Analysis Laboratory, Chalmers students Mr A. Jonsson and Mr V. Engdahl for initial synthesis, and Prof. Peter Svedlindh at Uppsala University for discussions.

Conflicts of interest

There are no conflicts to declare.

Notes and references

‡ **CTH-18** was prepared by solvothermal methods in dmf, and characterised by SCXRD, PXRD, TGA, SEM, gas sorption, magnetic and electrochemical measurements and elemental analysis. Topologies were analysed with ToposPro[32] and SYSTRE[33] and chemical stability tests were performed.

1 S. R. Batten, N. R. Champness, X.-M. Chen, J. Garcia-Martinez, S. Kitagawa, L. Öhrström, M. O'Keeffe, M. P. Suh and J. Reedijk, *Pure Appl. Chem.*, 2013, **85**, 1715–1724.
2 O. M. Yaghi, M. J. Kalmutzki and C. S. Diercks, *Introduction to Reticular Chemistry – Metal–Organic Frameworks and Covalent Organic Frameworks*, Wiley-VCH, Weinheim, 2019.
3 L. Öhrström and F. M. Amombo Noa, *Metal–Organic Frameworks*, American Chemical Society, 2021, DOI: 10.1021/acs.infocus.7e4004.
4 Z. Chen, M. C. Wasson, R. J. Drout, L. Robison, K. B. Idrees, J. G. Knapp, F. A. Son, X. Zhang, W. Hierse, C. Kühn, S. Marx, B. Hernandez and O. K. Farha, *Faraday Discuss.*, 2021, **225**, 9–69.
5 M. Chang, T. Yan, Y. Wei, J.-X. Wang, D. Liu and J.-F. Chen, *Chem. Mater.*, 2022, **34**, 9134–9143.
6 M. Åhlén, F. M. Amombo Noa, L. Öhrström, D. Hedbom, M. Strømme and O. Cheung, *Microporous Mesoporous Mater.*, 2022, **343**, 112161.
7 S. G. Dunning, N. K. Gupta, J. E. Reynolds, III, M. Sagastuy-Breña, J. G. Flores, E. Martínez-Ahumada, E. Sánchez-González, V. M. Lynch, A. Gutiérrez-Alejandre, J. Aguilar-Pliego, K.-S. Kim, I. A. Ibarra and S. M. Humphrey, *Inorg. Chem.*, 2022, **61**, 15037–15044.
8 Q.-X. Jia, Y.-Q. Wang, Q. Yue, Q.-L. Wang and E.-Q. Gao, *Chem. Commun.*, 2008, 4894–4896, DOI: 10.1039/B811865E.
9 C. Healy, K. M. Patil, B. H. Wilson, L. Hermanspahn, N. C. Harvey-Reid, B. I. Howard, C. Kleinjan, J. Kolien, F. Payet, S. G. Telfer, P. E. Kruger and T. D. Bennett, *Coord. Chem. Rev.*, 2020, **419**, 20.
10 F. M. Amombo Noa, M. Abrahamsson, E. Ahlberg, O. Cheung, C. R. Göb, C. J. McKenzie and L. Öhrström, *Chem*, 2021, **7**, 2491–2512.
11 P. T. K. Nguyen, H. T. D. Nguyen, H. Q. Pham, J. Kim, K. E. Cordova and H. Furukawa, *Inorg. Chem.*, 2015, **54**, 10065–10072.
12 F. M. Amombo Noa, E. Svensson Grape, S. M. Brülls, O. Cheung, P. Malmberg, A. K. Inge, C. J. McKenzie, J. Mårtensson and L. Öhrström, *J. Am. Chem. Soc.*, 2020, **142**, 9471–9481.
13 F. M. Amombo Noa, E. S. Grape, M. Åhlén, W. E. Reinholdsson, C. R. Göb, F.-X. Coudert, O. Cheung, A. K. Inge and L. Öhrström, *J. Am. Chem. Soc.*, 2022, **144**, 8725–8733.
14 M. Åhlén, A. Jaworski, M. Strømme and O. Cheung, *Chem. Eng. J.*, 2021, **422**, 130117.
15 S.-M. Wang, X.-T. Mu, H.-R. Liu, S.-T. Zheng and Q.-Y. Yang, *Angew. Chem., Int. Ed.*, 2022, **61**, e202207066.
16 M.-B. Kim, S.-J. Lee, C. Y. Lee and Y.-S. Bae, *Microporous Mesoporous Mater.*, 2014, **190**, 356–361.
17 M.-B. Kim, T.-U. Yoon, D.-Y. Hong, S.-Y. Kim, S.-J. Lee, S.-I. Kim, S.-K. Lee, J.-S. Chang and Y.-S. Bae, *Chem. Eng. J.*, 2015, **276**, 315–321.
18 E. S. Grape, H. Xu, O. Cheung, M. Calmels, J. Zhao, C. Dejoie, D. M. Proserpio, X. Zou and A. K. Inge, *Cryst. Growth Des.*, 2020, **20**, 320–329.
19 Z. Zheng, N. Hanikel, H. Lyu and O. M. Yaghi, *J. Am. Chem. Soc.*, 2022, **144**(49), 22669–22675.
20 R. Bagai and G. Christou, *Chem. Soc. Rev.*, 2009, **38**, 1011–1026.
21 V. Baron, B. Gillon, O. Plantevin, A. Cousson, C. Mathoniere, O. Kahn, A. Grand, L. Öhrström and B. Delley, *J. Am. Chem. Soc.*, 1997, **119**, 3500.
22 X. Wang, X. Liu, H. Rong, Y. Song, H. Wen and Q. Liu, *RSC Adv.*, 2017, **7**, 29611–29617.
23 H. Yuan, G. Yuming and L. Jiang, *New J. Chem.*, 2022, **46**, 5741–5750.
24 C. Yin, C. Pan, X. Liao, Y. Pan and L. Yuan, *ACS Appl. Mater. Interfaces*, 2021, **13**, 35837–35847.
25 K. Singh, J. d J. Guillen Campos, F. Dinic, Z. Hao, T. Yuan and O. Voznyy, *ACS Mater. Lett.*, 2020, **2**, 798–800.
26 A. Schoedel, M. Li, D. Li, M. O'Keeffe and O. M. Yaghi, *Chem. Rev.*, 2016, **116**, 12466–12535.
27 T. Grancha, X. Qu, M. Julve, J. Ferrando-Soria, D. Armentano and E. Pardo, *Inorg. Chem.*, 2017, **56**, 6551–6557.
28 T. Grancha, J. Ferrando-Soria, D. M. Proserpio, D. Armentano and E. Pardo, *Inorg. Chem.*, 2018, **57**, 12869–12875.
29 L. S. Xie, E. V. Alexandrov, G. Skorupskii, D. M. Proserpio and M. Dincă, *Chem. Sci.*, 2019, **10**, 8558–8565.
30 P. Tshuma, B. C. E. Makhubela, L. Öhrström, S. A. Bourne, N. Chatterjee, I. N. Beas, J. Darkwa and G. Mehlana, *RSC Adv.*, 2020, **10**, 3593–3605.
31 A. Lawson, World's 'most potent greenhouse gas' escaped during work on UK windfarm, The Guardian, 2022. https://www.theguardian.com/business/2022/nov/08/greenhouse-gas-uk-windfarm-seagreen-project-scotland.
32 V. A. Blatov, A. P. Shevchenko and D. M. Proserpio, *Cryst. Growth Des.*, 2014, **14**, 3576–3586.
33 O. Delgado-Friedrichs and M. O'Keeffe, *Acta Crystallogr., Sect. A: Found. Crystallogr.*, 2003, **59**, 351–360.